Surface Science xxx (2009) xxx–xxx

Contents lists available at ScienceDirect

Surface Science

journal homepage: www.elsevier.com/locate/susc

Atomic, electronic and thermodynamic properties of cubic and orthorhombic $LaMnO_3$ surfaces

Yu.A. Mastrikov [a,b], E. Heifets [a], E.A. Kotomin [a,b,*], J. Maier [a]

[a] Max Planck Institute for Solid State Research, Heisenbergstr. 1, D-70569 Stuttgart, Germany
[b] Institute for Solid State Physics, University of Latvia, Kengaraga str. 8, Riga LV-1063, Latvia

ARTICLE INFO

Article history:
Received 29 August 2008
Accepted for publication 20 November 2008
Available online xxxx

Keywords:
$LaMnO_3$
Surfaces
Ab initio calculations

ABSTRACT

We studied in detail the atomic and electronic structure of the $LaMnO_3$ surfaces, in both cubic and orthorhombic phases, combining GGA-plane wave approach, as implemented into the VASP-4.6.19 computer code, with a slab model. These studies are complemented by a thermodynamic analysis of the surface stability at different gas pressures and temperatures. The obtained results are compared with similar studies for other ABO_3-perovskites.

1. Introduction

The ABO_3-type perovskite manganites and cobaltates (A = La, Sr, Ca; B = Mn, Co) are important functional materials with numerous high-tech applications [1]. Some of them require understanding and control surface properties. An important example is $LaMnO_3$ (LMO) in its function as a cathode for solid oxide fuel cells (SOFC) [2–4]. LMO has a cubic structure above 750 K. Below this temperature the structure is orthorhombic, with four formula units in a primitive cell. Due to the high spin state of Mn^{3+} ion, LMO reveals several magnetic configurations. Below T_N = 140 K the A-type antiferromagnetic (AF) phase is the ground state. This corresponds to the ferromagnetic coupling in the basal *ab* (*xy*) plane combined with an antiferromagnetic coupling in the *c* (*z*) direction (in the *Pbnm* setting). There exist also other magnetic states: the ferromagnetic (FM) one, and the two antiferromagnetic GAF and CAF states. In the former all the spins are antiferromagnetically coupled to their nearest neighbors, whereas in the latter state the spins are antiferromagnetically coupled in the basal plane and ferromagnetically between the planes (along the *c* axis).

Understanding of the pure LMO-type surface properties is a necessary first step for the spintronic low-temperature applications and for establishing the mechanism of oxygen reduction on these surfaces which is a key issue in improving the performance of SOFC cathodes at high temperatures [1]. Several first-principle studies of the LMO surfaces were undertaken recently ([5] and the references therein). However, these studies were limited to the cubic structure, often for unrelaxed surfaces, and zero temperature. In this paper, we compare properties of cubic and orthorhombic LMO surfaces at high temperatures and realistic gas pressures. We discuss here three surfaces – (001), (110) and (111) – with different terminations and in different magnetic states described above for the bulk LMO. The main calculated properties include the surface energies, atomic displacements, effective charges, and the Gibbs free energies under different external conditions.

The plan of the paper is as follows. Section 2 deals with computational details, Section 3 describes results on the atomic and electronic structure, whereas the results of thermodynamic analysis are presented in Section 4. Conclusions are summarized in Section 5.

2. Computational details

In this study, we employed the VASP-4.6.19 computer code [6]. We used Perdew–Wang 91 GGA nonlocal exchange-correlation functional and the basis set of plane waves (PW). Due to open electronic shells on Mn ions, the spin-polarized calculations were performed. More details are given in Ref. [5]. We have demonstrated therein that the VASP code reproduces well the LMO lattice constants (in both phases with accuracy < 1%) as well as the cohesive energy and magnetic coupling constants. The effective atomic charges are calculated using the Bader (topological) analysis [7].

In our surface modeling, we used a slab model infinite in the two (*x*, *y*) dimensions and containing a finite number of planes

* Corresponding author. Address: Max Planck Institute for Solid State Research, Heisenbergstr. 1, D-70569 Stuttgart, Germany.
E-mail addresses: kotomin@latnet.lv, E.Kotomin@fkf.mpg.de (E.A. Kotomin).

0039-6028/$ - see front matter © 2008 Elsevier B.V. All rights reserved.
doi:10.1016/j.susc.2008.11.034

along the z axis normal to the surface. The orthorhombic surface unit cell has an area twice as large as for a cubic unit cell. A large vacuum gap of 15.8 Å between slabs periodically repeated along the z axis was used here, in order to prevent an interaction between the two surfaces through the vacuum region.

We started with the (001) surface, which exhibits the MnO_2/LaO/MnO_2/··· sequence of oppositely charged planes (±1e, assuming formal ionic charges: Mn^{3+}, La^{3+}, O^{2-}). Table 1 schematically shows two types of slabs used. The stoichiometric cubic 8-layer (with an even number of planes, in general) slab (a) consists of a four LMO formula units (each pair of neighboring planes gives a formula unit per unit area of surface). Its potential shortcoming is that this slab has a dipole moment normal to the surface, due to summation of the electrostatic fields of all planes [8,9]. Such a slab could be unstable with respect to reconstruction or defect formation. Alternatively, the dipole moment can be compensated by the charge redistribution near the surface (to be discussed below).

To get rid of the dipole moment, symmetrical slabs (Table 1b and c) are often used. Such slabs have an odd number of planes (typically seven in our calculations) and the same terminations on both sides, e.g., MnO_2 or LaO. This allows us to analyze independently the energy and other properties for different terminations (e.g., LaO and MnO_2). In particular, this is necessary for thermodynamic analysis of surface stability (Section 4). Despite the fact that these 7-plane slabs are not stoichiometric, but two symmetrical slabs with different terminations as put together contain an integer number of bulk unit cells.

Based on these considerations, two following relations are used for calculations of the cleavage energy. The average cleavage energy over two terminations for stoichiometric slabs is given by

$$E_{cl} = \frac{1}{2S} \cdot (E_{slab} - n \cdot E_{bulk}), \quad (1)$$

where S is an unit area of surface, E_{slab} is the total energy of the slab, n is corresponding number of the bulk units, E_{bulk} is the total energy of the bulk unit. As a reference, the total energies of the bulk unit cell for the corresponding structure and magnetic ordering were taken. The unit cell of the stoichiometric cubic 8-layer slab contains $n = 4$ formula units.

Table 1
Plane sequence for the (001) 8-plane (a) and 7-plane MnO_2-terminated (b) and LaO-terminated (c) slabs.

a	b	c
MnO_2	MnO_2	
LaO	LaO	LaO
MnO_2	MnO_2	MnO_2
LaO	LaO	LaO
MnO_2	MnO_2	MnO_2
LaO	LaO	LaO
MnO_2	MnO_2	MnO_2
LaO		LaO

For nonstoichiometric slabs E_{cl} is traditionally determined as [5,10]:

$$E_{cl} = \frac{1}{4S} \cdot (E_{t1} + E_{t2} - n \cdot E_{bulk}) \quad (2)$$

where E_{t1} and E_{t2} denote the total energies of the slabs with odd number of planes with complementary (e.g., LaO- and MnO_2-) terminations. Unit cells of two 7-layer slabs in cubic phase shown in columns b and c in Table 1 contain together $n = 7$ formula units. We compare below the results obtained using Eqs. (1) and (2).

When ions are frozen in their lattice positions and are not allowed to relax to the minimum of the total energy, we call this unrelaxed cleavage energy.

3. The atomic and electronic structure

3.1. The (0 0 1) surface

The (001) cleavage energies were calculated for the FM state in Ref. [5]. It is quite low and close to that for $SrTiO_3$(001) surfaces, viz. 1.2 eV [10]. The energies are saturated at slab thickness of 7–8 planes. The two different ways of cleavage energy calculations, using slabs with odd and even number of planes, Eqs. (1) and (2), gave similar results.

Thus, the 7- and 8-plane slabs were chosen here for further calculations of the cleavage energy for slabs with different magnetic ordering (Table 2). In some slab calculations the total magnetic moment was fixed (0 for all AF states and $4\mu_B$ per each Mn^{3+} ion in the FM state multiplied by a number of Mn ions in the supercell), whereas in other calculations, the magnetic moments were self-consistently optimized along with the electronic density distribution. The results practically do not depend on the initial guess of the magnetic moments.

As follows from Table 2, the considerable effect of magnetic moment optimization on the cleavage energy is seen only in the FM state with a relaxed geometry for both cubic and orthorhombic slabs (changed by 0.28 and 0.21 eV/a_0^2), whereas for AFM slabs this effect is negligible (<0.06 eV/a_0^2). In the FM case the optimized magnetic moments are $4 \pm 0.25\mu_B$ depending on the surface termination. For a comparison with a cubic structure, we calculated also the cleavage energy for the orthorhombic slab in the FM state. This energy exceeds that for a cubic slab in the same magnetic state by 0.14–0.21 eV. Note also that the FM slabs, both cubic and orthorhombic, show cleavage energy slightly larger than that for the AFM slabs.

Due to high symmetry, in the cubic phase only the z coordinate had to be varied. A full slab geometry optimization was performed for the orthorhombic phase. As a result, some minor atomic displacements in the planes parallel to the surface took place in the orthorhombic FM slab. The largest atomic displacements were observed again along the z axis, similarly to those in the cubic slabs. Full details of calculations are presented in Ref. [11]. We summa-

Table 2
Cleavage energies of the (001) surface (eV/a_0^2) for cubic slabs in different magnetic configurations.

Slab	7-Plane				8-Plane	
Total magnetic moment	Fixed		Optimised		Fixed	
	Unrelaxed	Relaxed	Unrelaxed	Relaxed	Unrelaxed	Relaxed
FM	1.60	1.25	1.55	0.97	1.61	0.87
AAF	1.53	0.95	1.53	0.94	1.51	0.77
CAF	1.46	1.01	1.43	0.95	1.46	0.78
GAF	1.34	0.76	1.34	0.75	1.43	0.61
FM[a]	1.84	1.39	1.77	1.18	1.77	1.13

[a] Orthorhombic slab.

Please cite this article in press as: Y.A. Mastrikov et al., Surf. Sci. (2009), doi:10.1016/j.susc.2008.11.034

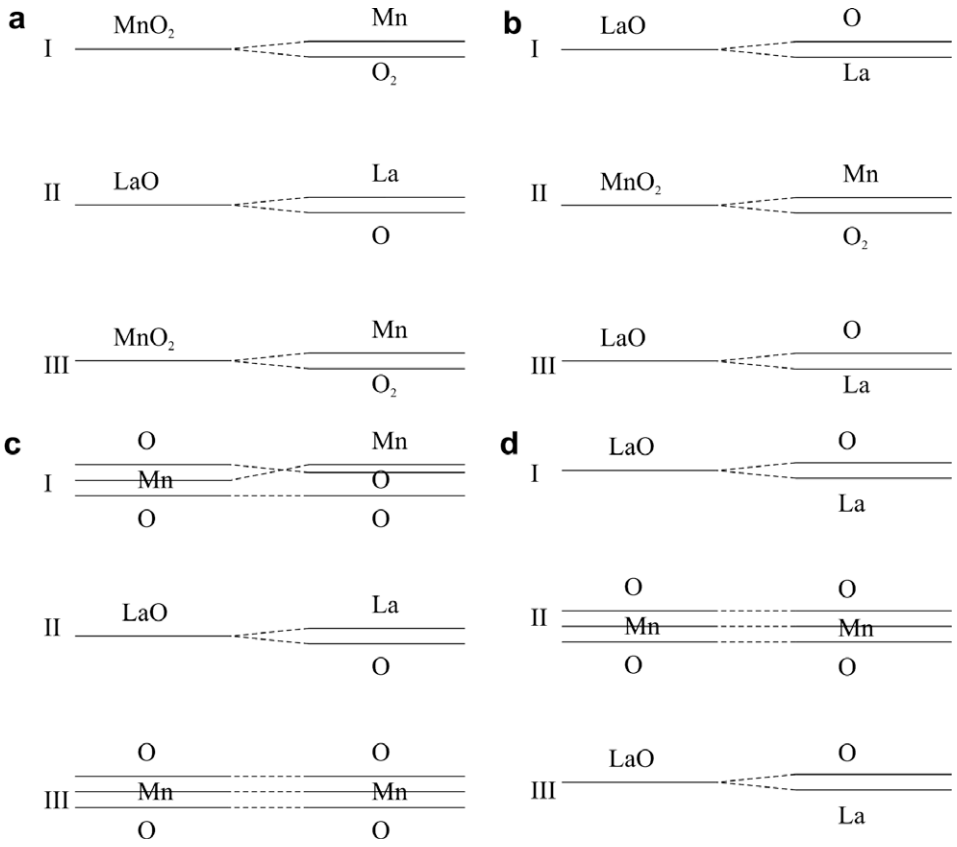

Fig. 1. Plane splitting in the (001) surfaces (right side) with respect to the bulk (left side) in cubic (a), (b), and orthorhombic (c), (d) slabs for MnO_2- (a), (c) and LaO-termination (b), (d).

rize here only the main results which are essential for the thermodynamic analysis in Section 4.

Changes in the slab geometry caused by its relaxation could be expressed in terms of the interplanar and Mn–O relative distances in the MnO_6 octahedra along the [001] direction perpendicular to the surface. In the cubic phase of LMO bulk, the optimized distance between the nearest MnO_2 and LaO planes is 1.95 Å (left side of Fig. 1a and b). However, near the two surface terminations these planes are split-off (right side of Fig. 1a and b). The splitting of the top plane is called rumpling. As a result, we obtained four most important different (interplanar) distances in the relaxed cubic slabs: the top Mn–O_2 plane rumpling, O_2–La distance, La–O plane splitting, and O–Mn distance between planes II and III (Fig. 1a and b). The rumpling of the MnO_2 and LaO surface planes in the cubic slabs is about 0.19 and 0.44 Å, respectively [11], which could be checked by means of LEED experiments. These distances vary, depending on the proximity to the surface or particular termination, which can be easily identified for the 8-plane slabs (Table 3). The Mn–O_2 plane splitting and Mn–O interplanar separation distance monotonically decrease and increase, respectively, when going along the [001] direction from the MnO_2- towards the LaO-termination. The interplane distance in the 8-plane slab center is very close to that in the bulk. Notice that Mn ions move always above O ions from the same plane whereas La ions move below O in LaO-, but above O ions in the MnO_2-termination.

Owing to the reduction of symmetry in the orthorhombic bulk, an MnO_2 plane splits off into three subplanes as shown in Fig. 1c and d (left side). The O–Mn distance along the [001] direction in the orthorhombic cell is 1.97 Å. The interplanar distance calculated for the orthorhombic bulk is (Fig. 1c and d): LaO(I)–O(II) 1.66 Å,

Table 3
The relative Mn–O distances (Å) along the [001] direction for 8- (a) and 7-plane (b) slabs, and their differences for these two slabs. The top plane (first row) corresponds to the MnO_2-termination whereas the bottom plane (last row) to LaO-termination.

MnO_2-termination														
8-Plane					7-Plane					Difference for 8- and 7-planes				
FM	AAF	CAF	GAF	FM[a]	FM	AAF	CAF	GAF	FM[a]	FM	AAF	CAF	GAF	FM[a]
2.12	2.12	2.12	2.13	2.09	2.10	2.12	2.11	2.12	2.07	0.02	0.00	0.01	0.01	0.02
1.88	1.88	1.87	1.87	1.85	1.88	1.85	1.87	1.85	1.84	−0.01	0.03	0.00	0.02	0.00
2.00	2.01	2.00	2.02	2.00	1.95	1.94	1.94	1.93	1.95	0.05	0.08	0.06	0.10	0.05
1.94	1.90	1.95	1.89	1.93	Mirror plane									
2.03	1.96	2.07	1.95	1.99	2.00	1.95	1.98	1.94	1.97	0.04	0.01	0.08	0.00	0.02
1.99	1.99	1.93	2.03	2.01	2.02	2.00	2.03	2.03	2.05	−0.04	−0.01	−0.11	0.00	−0.04
2.10	2.06	2.09	2.13	2.15	2.09	2.05	2.15	2.14	2.18	0.01	0.01	−0.06	−0.01	−0.03
LaO-termination														

[a] Orthorhombic slab.

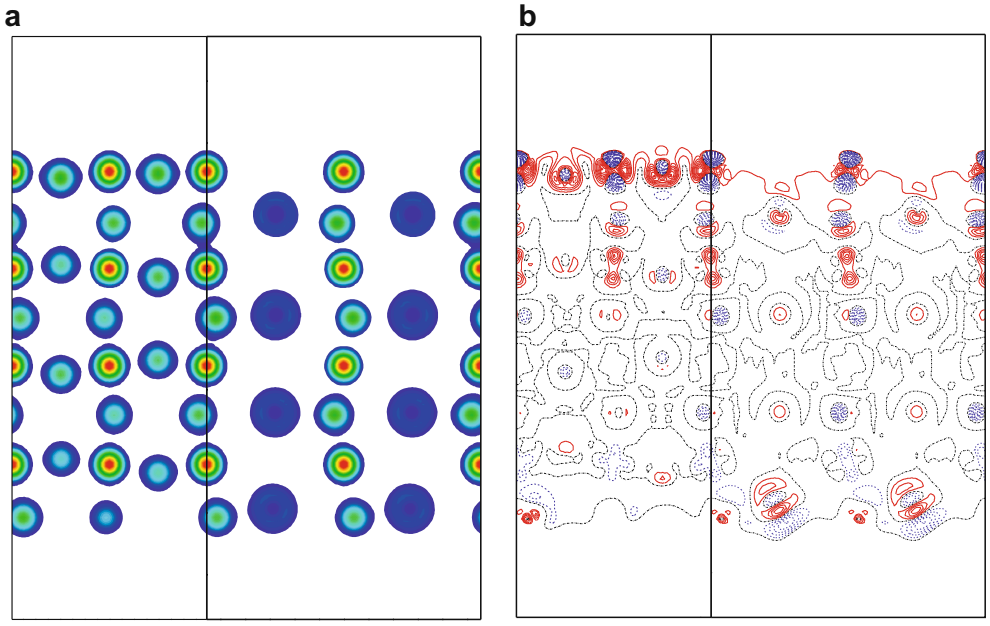

Fig. 2. Total (a) and difference (b) electron density maps for 8-plane slab. Solid red and dash blue lines in the difference (b) electron density map represent deficiency and excess of the electron charge, respectively. Density increment is $0.0125e/Å^3$. Dash-dot black line is the zero level.

while the splitting of plane II O–Mn is 0.31 Å. All calculated slabs with different magnetic orderings for the corresponding terminations demonstrate similar atomic displacements. There is a small difference between the relaxation in the odd-plane slabs near the mirror plane and that in the central planes of the even-layer slabs, caused by symmetry of the slabs. The MnO_2 plane splitting into three subplanes mentioned above arises due to the tilting of the MnO_6 octahedra. The sequence of the subplanes here is the same as in the bulk (O–Mn–O), except for the terminating MnO_2 plane. The Mn-subplane moves therein outwards from the slab center, leaving both top O subplanes below (Fig. 1c). The outward move of Mn ions from the MnO_2 plane on the MnO_2-terminated surfaces was also observed for the cubic slabs. However, for the LaO-termination La atoms are covered by O subplane. This is true for both 7- and 8-layer (0 0 1) slabs.

In order to illustrate the charge density redistribution upon surface formation and atomic relaxation in the stoichiometric 8-plane slab, the total and difference density maps (with respect to the bulk) are plotted in Fig. 2. The total density maps clearly show the zig-zag-type wavy orthorhombic structure of slabs. The difference maps demonstrate, in its turn, that only near-surface metal atoms are visibly perturbed (Mn atoms considerably polarized) and that there is no interaction between two terminating surfaces of a slab. A comparison with similar calculations for the symmetrical 7-plane slab shows that in spite of the different stoichiometry of the 7- and 8-plane slabs, this perturbation is very similar for the corresponding terminations of both slabs. This allows us to use computationally more feasible nonstoichiometric symmetrical 7-plane slabs in a further modeling of oxygen interaction with LMO surfaces.

To shed more light on the electronic density redistribution, the Bader effective atomic charges were calculated for 7- and 8- plane slabs in different magnetic states [11]. We found that the effective charges reveal considerable covalence of the Mn–O chemical bonding. The calculated charges depend weakly on the slab magnetic states.

The surface-induced perturbation is not restricted to the first plane as in semiconducting $SrTiO_3$ [10], rather for both terminations the perturbation remains considerable in several planes below the surface – in line with the results for the stoichiometric slab and previous HF calculations [12,13]. The effective atomic charges in the cubic and orthorhombic bulk phases are quite similar, 2.13*e* (2.07*e*) for La, 1.85*e* (1.68*e*) for Mn, and −1.29*e* (−1.25*e*) for O ions in the FM cubic (orthorhombic) phases, respectively. Charge redistribution in a cubic 7-plane slab with LaO-termination is limited mostly to the first two surface planes (compare the bulk charges above with 1.98*e* for La and −1.33*e* for O in the first layer and 1.63*e* for Mn, −1.31*e* for O in the second plane) whereas for the MnO_2-termination charge perturbation spread deeper, to the third plane [11].

A comparison of the two nonstoichiometric slabs (with MnO_2- and LaO-terminations on both sides) shows [11] that the deviations of the total slab charge with respect to the bulk are equal but have opposite signs (±0.66*e* for the FM state). The deviation of this charge from ±1*e*, which is expected for the formal ionic charges (O^{2-}, La^{3+}, Mn^{3+}), is due to the partial Mn–O bond covalency.

3.2. The (1 1 0) surfaces

The atomic and electronic structure of the polar (1 1 0) $LaMnO_3$ surfaces was calculated for the FM configuration and both cubic and orthorhombic phases. Similarly, both the 8-plane stoichiometric asymmetrical slabs O_2/LaMnO/···LaMnO and two types of 7-plane nonstoichiometric but symmetrical slabs without dipole moments (O_2/LaMnO···O_2 and LaMnO/O_2···LaMnO) were modeled as shown in Table 4.

The (1 1 0) O_2-terminated 7-plane slab could be made stoichiometric by removing from both terminating surfaces half of the O ions, i.e., leaving one O ion instead of the two in the surface unit cell. This procedure is widely used for stabilization of the polar oxide surfaces, e.g., for $SrTiO_3$(1 1 0) surface [9,14]. In our study, we used a 2×1 extended surface unit cell where we removed half of the O ions from the nearest surface cells in the zig-zag way [15], which corresponds to a larger distance between surface oxygen vacancies and lower surface energy. Eqs. (1) and (2) were used in calculations of the cleavage energy.

As follows from Table 5, the VASP-calculated cleavage energies needed for creation of defect-free (0 1 1) surfaces practically coincide irrespective of whatever 7- or 8-layer slabs were used to esti-

Table 4
The plane sequence for the (1 1 0) surface modeled using 8-plane (a), 7-plane LaMnO- (b), O_2- (c), and O- (d) terminated slabs.

a	b	c	d
LaMnO	LaMnO		
O_2	O_2	O_2	O
LaMnO	LaMnO	LaMnO	LaMnO
O_2	O_2	O_2	O_2
LaMnO	LaMnO	LaMnO	LaMnO
O_2	O_2	O_2	O_2
LaMnO	LaMnO	LaMnO	LaMnO
O_2		O_2	O

Table 5
Cleavage energies of the FM (1 1 0) surface (in eV/a_0^2).

Slab	Surface type	Cubic		Orthorhombic	
		Unrelaxed	Relaxed	Unrelaxed	Relaxed
8-Plane	Defect-free	2.60	1.69	2.70	1.75
7-Plane	Defect-free	2.59	1.29	2.69	1.80
	O-term, symmetrical	1.59	0.75	1.68	0.96
	O-term, asymmetrical	1.60	0.49	1.68	0.76

mate these energies. The cleavage energy for the defect-free (0 1 1) surfaces is larger than that for the above discussed (0 0 1) surface. The same conclusion was drawn in the HF calculations [12]. It is very important that the calculated cleavage energy needed for creation of (0 1 1) surfaces with one half of the O atoms removed is considerably lower than the cleavage energy for the defect-free (0 1 1) surfaces. It appears that the cleavage energy for O-terminated (0 1 1) surface is even smaller than the one for (0 0 1) surfaces in the same FM state. In other words: the removal of a half of the O atoms from the polar (1 1 0) surface has indeed a strong stabilizing effect. A similar conclusion was drawn earlier based on the shell model and unrelaxed HF calculations [12,15].

We have compared the atomic relaxations for 7- and 8-plane slabs [11]. Unlike the (0 0 1) surface, atoms in O_2 planes now experience (even without defects) in-plane displacements along the *y* axis. Moreover, we observe large surface La displacements inwards the slab center (6–7% of a_0), whereas Mn and O ions move in the opposite direction. As a result, we predict that this surface must exhibit very large rumpling, which could be checked by means of LEED experiments. The variation in atomic displacements observed here for 7- and 8-plane slabs arises likely due to a considerable dipole moment in the latter case characteristic for the strongly polar (1 1 0) surface. This is in line with our similar conclusions for the (1 1 0) $SrTiO_3$ [16]. Lastly, the atomic relaxations on the O-terminated (1 1 0) surfaces containing O atoms in the two possible configurations show that the removal of O atoms from the surface induces considerable (~10%) in-plane and inward atomic displacements.

Analysis of the effective charges [11] demonstrates that for both 8-layer as well as 7-layer slabs the top layer of the LaMnO-terminated surface with respect to the bulk is strongly negatively charged (−0.82*e* and −1.14*e*, respectively). The charge of the first subsurface layer is much closer to that of the bulk. With respect to the bulk the top layers of the O_2-terminated surfaces are less negatively charged (by 0.51*e* for 8-layer slab and by 0.79*e* for the 7-layer slab). At the O-terminated surface, regardless of the arrangement of the surface O atoms, terminating layers are positively charged with respect to O_2 planes the bulk by 1.44*e*, which is close to a half of the charge on O_2 planes in the LMO bulk.

Table 6
The (1 1 1) cleavage energy in a cubic phase (eV/a_0^2).

		Unrelaxed	Relaxed
7-Plane	Defectless	2.77	2.68
	$Mn_{0.5}$		2.07
8-Plane	Defectless	2.80	2.74

3.3. The (1 1 1) surface

We calculated also the cleavage energies for the 7- and 8-plane (1 1 1) surfaces with Mn- and LaO_3-terminations (Table 6). The main conclusion is that this energy is much larger than that for the (0 0 1) surface. The energy estimates based on Eqs. (1) and (2) are very close. Removal of half of the Mn atoms from Mn-terminated surface stabilizes the surface but not enough to compete with the (0 0 1) cleavage energy.

4. Thermodynamic treatment of surface stability

4.1. General analysis

In order to determine stabilities of different surfaces under varying environmental conditions (such as partial oxygen pressure and temperature), we applied here the thermodynamic formalism which we used earlier for $BaZrO_3$ [17] and $SrTiO_3$ [10] perovskites. This analysis is based on a general *ab initio* thermodynamics approach (see [18–23] and references therein for details). Only symmetrical slabs were used in this analysis.

We assume the equilibrium between the slab surface and the bulk perovskites with respect to exchange of atoms. This means that for surface the usual relation between the chemical potentials of three crystal constituents (La, Mn, and O) holds:

$$\mu_{\mathrm{La}} + \mu_{\mathrm{Mn}} + 3\mu_{\mathrm{O}} = \mu^0_{\mathrm{LaMnO_3}} \approx E^{\mathrm{bulk}}_{\mathrm{LaMnO_3}}, \tag{3}$$

where $\mu^0_{\mathrm{LaMnO_3}}$ denotes the chemical standard potential of the $LaMnO_3$ phase, $E^{\mathrm{bulk}}_{\mathrm{LaMnO_3}}$ the total energy per formula unit in a LMO crystal, and μ_{La}, μ_{Mn}, and μ_{O} the chemical potentials of three constituents, respectively. We neglect the vibrational contribution into the Gibbs free energy since this is typically quite small [18]. Moreover, an accurate account of these effects is very difficult and extremely time-consuming due to necessity to calculate phonon spectra for perovskite surfaces. Because the chemical potentials of three components are interrelated by Eq. (3), only two of these chemical potentials are independent variables. Because O atoms are in equilibrium on the surface and in the O_2 gas above the surface and we have to account for a strong dependence of O chemical potential on the O_2 gas partial pressure and temperature, it is suitable to choose the O chemical potential μ_{O} as one of independent variables in the surface Gibbs free energy whereas the Mn chemical potential μ_{Mn} can be taken as another independent variable.

The analysis of relative stability among different surfaces should account for a possible exchange with ions between surface and environment. In this case a principal energy characteristic is the excess surface Gibbs free energy (ESGFE) for the symmetrical slabs terminated on both sides with surfaces *i* (e.g., *i* = MnO_2 and LaO for the (0 0 1) surfaces)

$$\Omega^i = \phi^i_{\mathrm{La}} - \Gamma^i_{\mathrm{La,Mn}}\Delta\mu_{\mathrm{Mn}} - \Gamma^i_{\mathrm{La,O}}\Delta\mu_{\mathrm{O}}. \tag{4}$$

Here the excess of components *a* in the *i*-terminated surface with respect to the number of La ions in slabs is defined as (see, e.g., Ref. [19])

$$\Gamma^i_{\mathrm{La},a} = \frac{1}{2}\left(N^i_a - N^i_{\mathrm{La}}\frac{N^{\mathrm{bulk}}_a}{N^{\mathrm{bulk}}_{\mathrm{La}}}\right), \tag{5}$$

where N^i_a and N^{bulk}_a are the numbers of atoms *a* in slabs and in the bulk of the perovskite. The factor ½ in Eq. (5) accounts for two

surfaces in a slab. The deviation of chemical potential of Mn atom is calculated with respect to the total energy E_{Mn}^{bulk} per Mn atom in the bulk metal:

$$\Delta\mu_{Mn} = \mu_{Mn} - E_{Mn}^{bulk}. \quad (6)$$

The same deviation for O atom is considered with respect to the energy of O atoms in a O_2 molecule:

$$\Delta\mu_O(T,p) = \mu_O(T,p) - \frac{1}{2}E_{O_2} \quad (7)$$

Finally, the constants ϕ^i can be calculated from

$$\phi_{La}^i = \frac{1}{2}\left[E_{slab}^i - N_{La}^i E_{LaMnO_3}^{bulk}\right] - \Gamma_{La,Mn}^i E_{Mn}^{bulk} - \frac{1}{2}\Gamma_{La,O}^i E_{O_2}, \quad (8)$$

Table 7
Calculated formation energies ΔE_f (eV) for bulk La_2O_3, Mn_2O_3, MnO, MnO_2, and Mn_3O_4 oxides and $LaMnO_3$ perovskite. The third column contain experimental data [23] at $T^0 = 298.15$ K, $p^0 = 1$ atm, whereas the last column contains the same values extrapolated to $T = 0$ K, $p^0 = 1$ atm. The calculated LMO formation energies before brackets are for the orthorhombic phase, while values in brackets are for the cubic phase.

Crystal	Calculated ΔE_f	ΔH_0^f	ΔH^f ($T = 0$ K)
La_2O_3	−18.86	−18.60	−18.64
Mn_2O_3	−11.57	−9.92	−9.96
MnO	−4.19	−3.99	−4.00
MnO_2	−7.03	−5.39	−5.41
Mn_3O_4	−16.70	−14.37	−14.41
$LaMnO_3$	−15.91 (−15.66)	−14.77	−14.77
$LaMnO_3$ (from La_2O_3 and Mn_2O_3 oxides)	−0.75 (−0.50)	−0.514	−0.47

where E_{slab}^i is the total energy (per unit cell) for a slab terminated with surfaces i and $E_{LaMnO_3}^{bulk}$ is the total energy (per formula unit) in the LMO bulk.

The most stable surface composition and geometry is that which minimizes the ESGFE. The boundaries between stability regions for different surfaces i and j can be found in a straightforward way by solving the equations

$$\Omega^i(\Delta\mu_O, \Delta\mu_{Mn}) = \Omega^j(\Delta\mu_O, \Delta\mu_{Mn}). \quad (9)$$

The ESGFE for the most stable surface l has to be positive, otherwise the surfaces spontaneously appear and the crystal disintegrates. The boundary, where disintegration happens, is determined then by the equation

$$\Omega^l(\Delta\mu_O, \Delta\mu_{Mn}) = 0. \quad (10)$$

We assume then that a crystalline surface is in equilibrium with the bulk and with oxygen gas in surrounding environment. We consider only conditions under which a LMO crystal and its surface can exist and there is no precipitation of Mn and La metals and their oxides. These conditions lead to the following bounds on the chemical potentials of Mn and O atoms:

$$\Delta\mu_{Mn} \leqslant 0, \quad (11)$$

$$\Delta\mu_{Mn} + 3\Delta\mu_O \geqslant \Delta g_f(LaMnO_3) \quad (12)$$

$$x\Delta\mu_{Mn} + y\Delta\mu_O \leqslant \Delta g_f(Mn_xO_y) \quad (13)$$

$$2\Delta\mu_{Mn} + 3\Delta\mu_O \geqslant 2\Delta g_f(LaMnO_3) - \Delta g_f(La_2O_3) \quad (14)$$

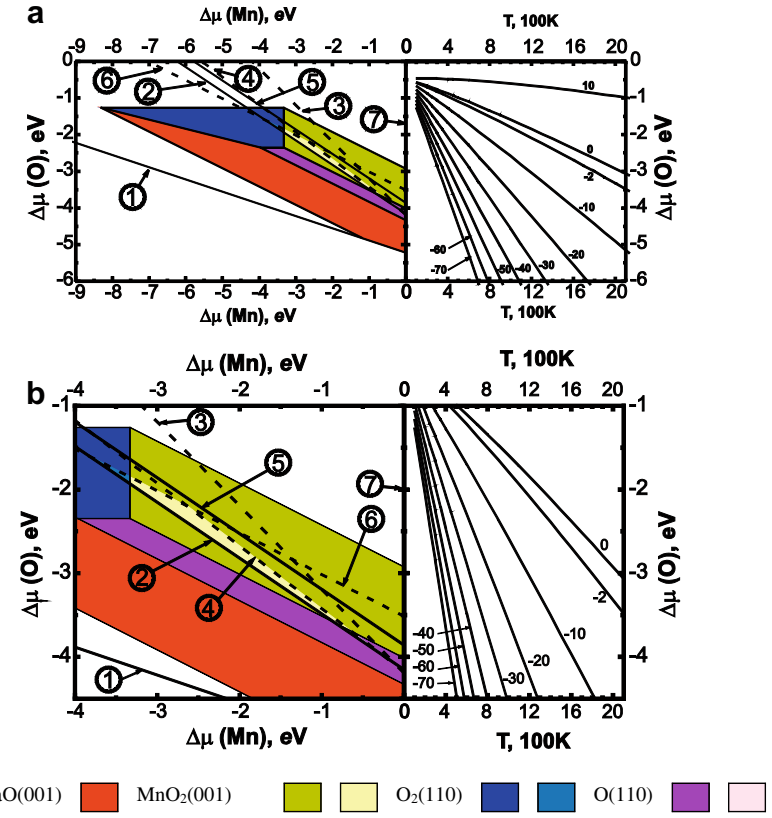

Fig. 3. Phase diagrams: the regions of stability of $LaMnO_3$ (in the cubic phase) surfaces with different terminations (LaMnO-, O_2-, and O-terminated (011) surfaces, LaO- and MnO_2-terminated (001) surfaces, as functions of chemical potential variations for manganese and oxygen atoms. Parameters for all lines on the left side of the figures are collected in Tables 7 and 8. The numbers in circles points to lines, where metals or their oxides begin to precipitate: (1) metal La, (2) La_2O_3, (3) MnO, (4) Mn_3O_4, (5) Mn_2O_3, (6) MnO_2, and (7) metal Mn. The right side of the figures contains a family of $\Delta\mu_O$ as functions of temperature at various oxygen gas pressures according to Eq. (17). The labels m on the lines represent the pressure: $p_{O_2} = 10^m$ atm. (a) Overall phase diagram; and (b) zoomed fragment with the LMO stability region.

Please cite this article in press as: Y.A. Mastrikov et al., Surf. Sci. (2009), doi:10.1016/j.susc.2008.11.034

where

$$\Delta g_f(\mathrm{LaMnO_3}) = E^{\mathrm{bulk}}_{\mathrm{LaMnO_3}} - E^{\mathrm{bulk}}_{\mathrm{La}} - E^{\mathrm{bulk}}_{\mathrm{Mn}} - \frac{3}{2}E_{\mathrm{O_2}} \quad (15)$$

and

$$\Delta g_f(\mathrm{M_xO_y}) = E^{\mathrm{bulk}}_{\mathrm{M_xO_y}} - xE^{\mathrm{bulk}}_{\mathrm{M}} - \frac{y}{2}E_{\mathrm{O_2}} \quad (16)$$

are the formation energies for $LaMnO_3$ and metal oxides.

We do not consider vibrational and pV contributions to the Gibbs free energy, which are supposed to be small [18]. This allows us to replace the Gibbs free energies for solids with the total energies obtained in the electronic structure computations. Since the dependencies of the chemical potentials of solids on the temperature and pressure are relatively weak [18], we neglected these effects in the present consideration. However, the oxygen gas free Gibbs energy is very sensitive to changes in temperature and/or oxygen gas partial pressure. Following [10,17–19], we used the experimental thermodynamical data [24] for oxygen gas in our analysis. Variation of the chemical potential for oxygen atom is

$$\Delta\mu_{\mathrm{O}}(T,p) = \frac{1}{2}\left\{\Delta G^{\mathrm{gas}}_{\mathrm{O_2}}(T,p^0) + kT\ln\left(\frac{p}{p^0}\right)\right\} + \delta\mu^0_{\mathrm{O}}. \quad (17)$$

$\Delta G^{\mathrm{gas}}_{\mathrm{O_2}}(T,p^0)$ here is the change in the O gas Gibbs free energy at the standard pressure p^0 = 1 atm and temperature T with respect to that at T^0 = 298.15 K

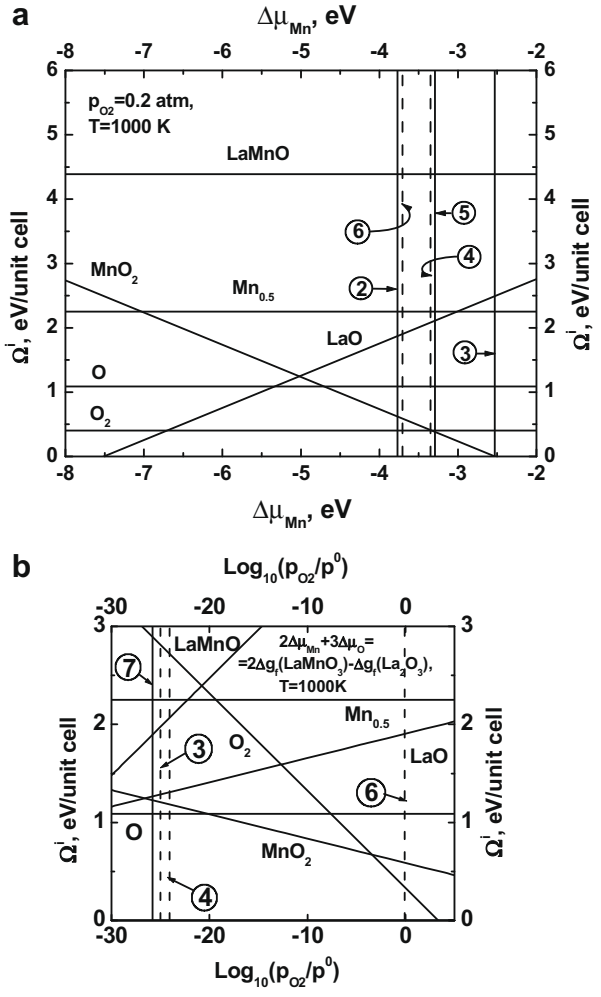

Fig. 4. ESFGEs for LMO in cubic phase: (a) as functions of $\Delta\mu_{\mathrm{Mn}}$ at T = 1000 K and p = 0.2 atm; (b) as functions of $\log_{10}(p_{\mathrm{O_2}}/p^0)$ at T = 1000 K for $2\Delta\mu_{\mathrm{Mn}} + 3\Delta\mu_{\mathrm{O}} = 2\Delta g_f(\mathrm{LaMnO_3}) - \Delta g_f(\mathrm{La_2O_3})$ (along the La_2O_3 precipitation line). Line numbers are the same as in Fig. 3.

$$\Delta G^{\mathrm{gas}}_{\mathrm{O_2}}(T,p^0) = G^{\mathrm{gas}}_{\mathrm{O_2}}(T,p^0) - G^{\mathrm{gas}}_{\mathrm{O_2}}(T^0,p^0). \quad (18)$$

This function is available from the standard thermodynamical tables [24]. The second term on right hand side of Eq. (17) describes dependence on a gas pressure within an ideal gas approximation. The last term in Eq. (17) matches the origin point of experimentally determined variation of the O atom chemical potential to coincide with the reference state in our theoretical analysis. This correction was estimated from the calculated energies of a metal M, its oxide M_xO_y, and experimental data for oxygen gas entropy $S^{\mathrm{gas}}_{\mathrm{O_2}}(T^0,p^0)$ and formation enthalpy $\Delta H^0_{f,\mathrm{M_xO_y}}$ for the metal oxide at the same standard conditions (T^0, p^0) using the relation

$$\delta\mu^0_{\mathrm{O}} = \frac{1}{y}\left(E_{\mathrm{M_xO_y}} - xE_{\mathrm{M}} - \Delta H^0_{f,\mathrm{M_xO_y}}\right) - \frac{1}{2}\left(E_{\mathrm{O_2}} + T^0 S^{\mathrm{gas}}_{\mathrm{O_2}}\left(T^0,p^0\right)\right). \quad (19)$$

The above-described analysis allows us to plot a phase diagram describing areas of stability of different crystal surfaces with respect to varying chemical potentials, in terms of easy accessible and manageable environment variables (T, p).

4.2. Results of surface analysis

The first step needed to perform a stability analysis for different crystal surfaces is to calculate the cohesive energies of the elemental metals, oxygen molecule and the formation energies for related metal oxides. The obtained values for metal cohesive energies [−4.25 eV for La and −2.77 eV for Mn] are consistent with experimental values [−4.47 and −2.92 eV, respectively] [25]. The calculated binding energy for O_2 molecule is 5.9 eV (vs. experimental value of 5.12 eV [26]). The results for the oxide formation energies are summarized in Table 7, where these are also compared with experimental formation enthalpies. Our computations overestimate the formation energies, which is commonly obtained with the GGA functionals. The difference between the calculated and the experimental formation energies depend on a number of

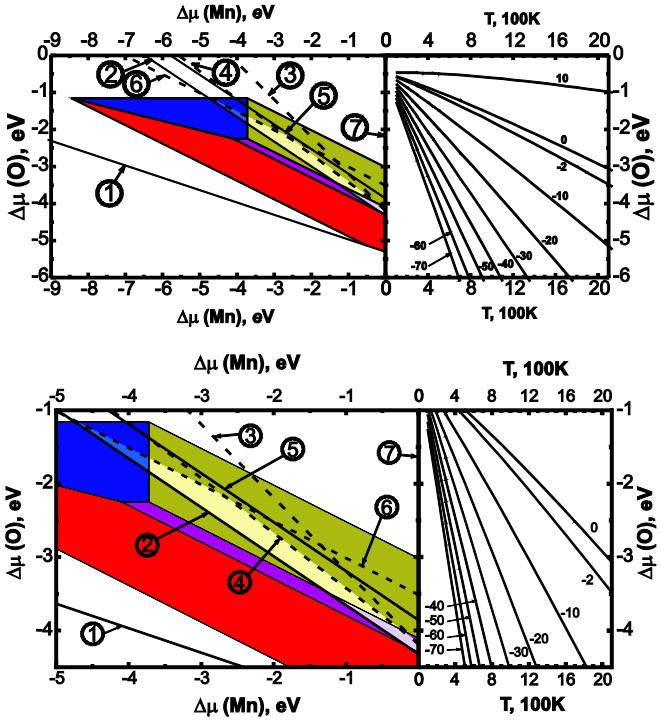

Fig. 5. Phase diagram: the same as Fig. 3 for $LaMnO_3$ in orthorhombic phase.

oxygen atoms in the formula units of oxides. This reflects the known DFT difficulty in a description of charge transfer processes. However, the LMO formation energy from oxides with the same oxidation numbers matches the experimental data very well. The calculated oxide formation energies were used to determine domains in the phase diagrams (Figs. 3 and 5), where the $LaMnO_3$ crystal is stable against the precipitation of metals and their oxides (according to Eqs. (11)–(14)).

As mentioned above, the LMO has two phases: low-temperature orthorhombic and high-temperature cubic (perovskite) structure. Therefore, we draw the surface phase diagrams (Figs. 3–6) for both phases, except for the slab with O-terminated (1 1 0) where it was impossible to retain a cubic symmetry. Therefore, similarly to Ref. [21], we used corresponding value of ϕ^i_{La} obtained for orthorhombic phase.

The ESGFE parameters, Eq. (4) for all LMO surfaces studied here are collected in Table 8. Parameters ϕ^i_{La} are calculated using Eq. (8), where all energies were obtained from our quantum-mechanical computations. The presented data are sufficient to analyze relative stability of different surfaces. According to a regular thermodynamical criterion, the most stable surface for any considered oxygen and manganese chemical potentials has the smallest ESGFE. Applying this criterion, we plotted the phase diagram (the left side of Figs. 3 and 5) showing where different surfaces of LMO are stable. The colored areas in both figures are limited at the bottom by the border lines, below which the chemical potential of La atoms in LMO exceeds that in La metal, corresponding to a precipitation of La atoms. On the other boundaries the colored area is limited by lines where the lowest ESGFE becomes negative. These lines are defined by Eq. (10).

Table 8
Parameters defining the surface Gibbs energies as functions of O and Mn chemical potentials: excesses $\Gamma^i_{La,O}$ and $\Gamma^i_{La,Mn}$ of O and Mn atoms in the surfaces with respect to the La atoms (5) and free energy of formation ϕ^i_{La} (8) at $\Delta\mu_O = \Delta\mu_{Mn} = 0$ eV for the $LaMnO_3$(001) surfaces under consideration. Values of ϕ^i_{La} (without brackets) are for the orthorhombic phase, values in brackets are for the cubic phase.

Surface		$\Gamma^i_{La,O}$	$\Gamma^i_{La,Mn}$	ϕ^i_{La} (eV/unit cell)	ϕ^i_{La} (J/m^2)
Orientation	Termination				
(001)	LaO	−1	−0.5	5.38 (5.42)	5.67 (5.70)
(001)	MnO_2	1	0.5	−3.02 (−2.93)	−3.18 (−3.08)
(110)	LaMnO	−1	0	6.13 (6.05)	4.56 (4.51)
(110)	O_2	1	0	−1.16 (−1.26)	−0.86 (−0.94)
(110)	O	0	0	1.09	0.81
(111)	LaO_3	0	−0.5	− (60.67)	− (45.19)
(111)	Mn	0	0.5	− (50.55)	− (37.65)
(111)	$Mn_{0.5}$	0	0	− (2.25)	− (1.67)

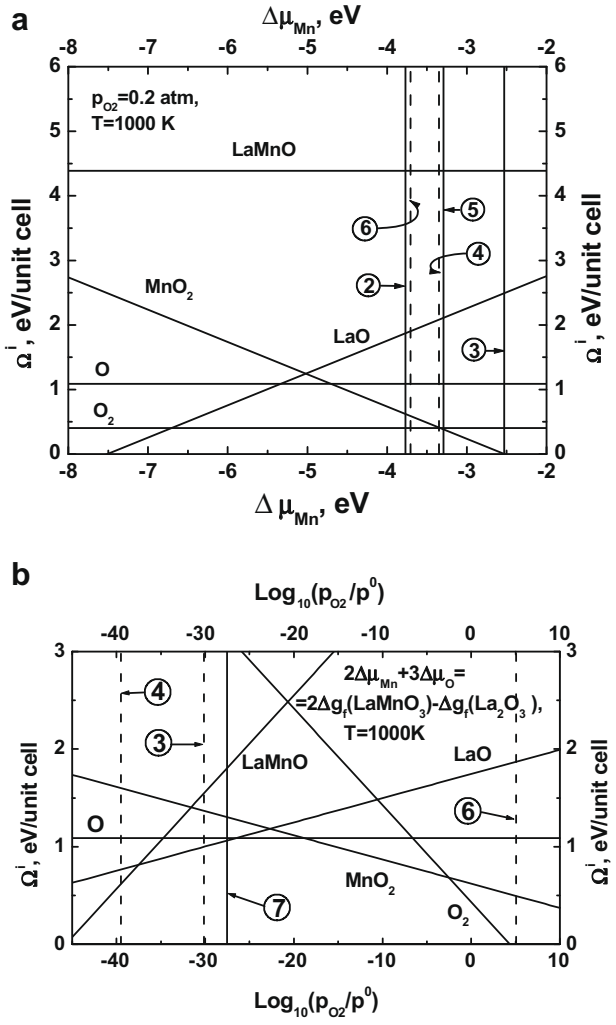

Fig. 6. ESFGEs for LMO in orthorhombic phase: (a) as functions of $\Delta\mu_{Mn}$ at $T = 1000$ K and $p = 0.2$ atm; (b) as functions of $\log_{10}(p_{O_2}/p^0)$ at $T = 1000$ K for $2\Delta\mu_{Mn} + 3\Delta\mu_O = 2\Delta g_f(LaMnO_3) - \Delta g_f(La_2O_3)$ (along the La_2O_3 precipitation line). Line numbers are the same as in Fig. 3.

The inequalities (11)–(14) determine the conditions under which the LMO crystal is stable with respect to disintegration into metals and their oxides. These conditions are represented in Figs. 3–6 by lines 1–7. The LMO surfaces can exist only while these conditions are fulfilled. The stability region for a cubic phase (Fig. 3) is limited by the line 2 (precipitation of La_2O_3) on the bottom and by the lines 4 and 6 (precipitation of Mn_3O_4 and MnO_2, respectively) on the top. Because of deficiencies in DFT descriptions of relative energies for materials with different degree of oxidation, we treat the obtained data with some caution and highlight the precipitation lines for 3-valent metal oxides La_2O_3 and Mn_2O_3 (solid lines 2 and 5). Of all considered surfaces, only three are stable within the region of the LMO crystal stability in the cubic phase: (i) O_2-terminated (1 1 0) surface in a small area at high O chemical potentials (O-rich limit) and low Mn chemical potential (Mn-poor limit), (ii) MnO_2-terminated (1 0 0) surface at the intermediate values of Mn and O chemical potentials, and (iii) O-terminated (1 1 0) surface in a small area at low O chemical potentials (O-poor limit) and high Mn chemical potential (Mn-rich limit). This result remains the same, no matter whether we consider only conditions Eqs. (13) and (14) for 3-valent oxides or add also conditions (13) for all other manganese oxides. However, the region of stability of MnO_2-terminated (1 0 0) surface reaches Mn metal precipitation line, if we limit our consideration only by a precipitation of 3-valent oxides.

The stability region for the orthorhombic phase (Fig. 5) is wider because LMO in this phase is more stable and the energy gain due to LMO formation phase is larger (Table 7). This shifts line 2 in Figs. 5 and 6 (Eq. (14)) to the left. The result of the extension of the area of LMO stability is a significant increase of the stability area for O_2- and O-terminated (1 1 0) surfaces on the opposite sides of the LMO stability region. The stability region of O-terminated (1 1 0) surface reaches the Mn precipitation line even if we take precipitation of all oxides into consideration. Also, the LaO-terminated (0 0 1) surface becomes stable within a very small area at the very edge of the Mn-rich and O-pure side of the stability region.

To unfold dependencies of the O chemical potential on the temperature and oxygen gas partial pressure and thus to show the dependence of the surface stability from these variables, we have drawn the functions Eq. (17) on the right hand side of Figs. 3 and 5. Consistent positioning of these experimental curves with respect to our computed stability diagram requires us to account for the correction, Eq. (19). We used the average value of these corrections

Table 9
The chemical potential correction (eV), Eq. (19), calculated for different oxides. The last line gives the average correction used in plotting the oxygen chemical potentials on right hand side of the phase diagrams in Figs. 3 and 5.

Crystal	Calculated $\delta\mu_O^0$
La_2O_3	−0.41
Mn_2O_3	−0.87
MnO	−0.52
MnO_2	−1.14
Mn_3O_4	−0.90
Average	−0.77

calculated for different oxides, when drawing the right side of Figs. 3 and 5. It was calculated using the same set of oxides as above in this study (Table 9). Both the values and the scattering of calculated corrections are much larger than in our previous similar studies [10,17–19] for non-magnetic oxides (e.g., $SrTiO_3$). We consider manganese oxides which are spin-polarized solids. We also included several Mn oxides with various degree of oxidation. In both cases the DFT faces well-known difficulties. The stability diagram, together with plotted dependencies of oxygen chemical potential, allow for a much more detailed understanding of changes in the surface stability under variation of the most important environmental conditions – temperature and oxygen gas partial pressure. Oxygen-rich conditions with a larger O chemical potential correspond to higher oxygen gas partial pressures and/or lower temperatures; oppositely, oxygen-pure conditions with the lower O chemical potentials correspond to smaller oxygen gas partial pressures and/or higher temperatures.

An additional insight on the ESGFE behavior could be obtained from Figs. 4 and 6, where we have plotted ESGFEs for all studied surfaces (i) under the partial pressure of oxygen gas in air, $p = 0.2$ atm (Figs. 4a and 6a), and (ii) along the La_2O_3 precipitation line (Figs. 4b and 6b). All ESGFEs on these figures are plotted at $T = 1000$ K. Fig. 4 is drawn for LMO in a cubic phase whereas Fig. 6 describes the LMO in an orthorhombic phase. For an oxygen partial pressure $p = 0.2$ atm the stability region lies between lines 2 (precipitation of La_2O_3) and 6 (precipitation of MnO_2). Only the O_2-terminated (1 1 0) surface is stable within this range in both phases. In the cubic phase (Fig. 4a), the MnO_2-terminated surface becomes more stable just before line 5 (precipitation of Mn_2O_3). In the orthorhombic phase (Fig. 6a) the area between lines 2 and 6 is much wider and the MnO_2-terminated (1 1 0) surface becomes more stable, very close to the line 6 (MnO_2 precipitation). The ESGFEs stability region drawn along the La_2O_3 precipitation line (Figs. 4b and 6b) lies between the lines 4 (Mn_3O_4 precipitation) and 6 (MnO_2 precipitation) for the cubic phase. The O-terminated (1 1 0) surface is stable on the low-pressure side of this region. Then the MnO_2-terminated (0 0 1) surface becomes more stable under intermediate pressures, and the O_2-terminated (1 1 0) surface is the most stable at the high-pressure side of the stability region. In the orthorhombic phase the lines 3 and 4 cross the line 1 (La_2O_3 precipitation) beyond the line 7 (Mn precipitation). Therefore, the stability region for the orthorhombic phase is limited by the Mn precipitation line on the low-pressure side. The same surfaces are stable along this path in the orthorhombic phase. In addition, the LaO-terminated surface becomes stable within a very small fragment at the low-pressure edge of the stability region.

5. Conclusions

We performed here the DFT study of the electronic and atomic structures of surfaces of the $LaMnO_3$ crystal, for both high-temperature cubic and low-temperature orthorhombic phases. The obtained data allowed us to compare stabilities of the surfaces under various environmental conditions determining variable chemical potentials of constituent metal atoms, temperatures and partial pressure of oxygen gas. Specific conclusions are as follows:

(1) Based on our calculations, we predict a large rumpling of the LMO (0 0 1) surface. This could be checked by means of LEED experiments.
(2) The calculated Mn–O distances along the z axis show that the upper parts of MnO_6 octahedra are regularly expanded whereas the lower parts as compressed as compared to the perfect bulk MnO_6 octahedron.
(3) There is a considerable electronic density redistribution near the surface which could affect atomic and molecular adsorption (corresponding simulations are in progress). The calculated effective atomic charges weakly depend on the magnetic structure and slab stoichiometry.
(4) The (1 1 0) surface is stabilized by a partial removal of oxygen ions from the surface, similarly to $SrTiO_3$ [14]. This surface has the lowest cleavage energy and demonstrates even larger rumpling and deeper perturbation with respect to the bulk and in-plane ionic displacements, unlike the (0 0 1) surface. The cleavage energies for the (1 1 1) and the stoichiometric (1 1 0) surfaces are larger than that for the (0 0 1) and O-terminated (0 1 1) surfaces.
(5) Thermodynamic analysis demonstrates that the O-terminated (0 1 1) surface in both cubic and orthorhombic phases is stable only under very poor O- and Mn-conditions. However, under SOFC operational conditions O_2-terminated (0 1 1) and MnO_2-terminated (0 0 1) surfaces are the most thermodynamically stable.

These results are important for the further modeling of the LMO surface interaction with oxygen atoms and molecules relevant for the catalysis and fuel cell applications [11,27]. Notice that our approach is suitable for both stoichiometric and nonstoichiometric surfaces, including, e.g., possible segregation of Sr dopant, O vacancies or MnO_2 phase towards the (Sr, La)MnO_3 surface. These problems will be discussed in upcoming papers.

Acknowledgements

This study was partly supported by the Latvian National Program on Material Science. We thank R. Evarestov, S. Piskunov and D.S. Mebane for stimulating discussions.

References

[1] C. Israel, M.J. Calderon, N.D. Mathur, Mater. Today 10 (2007) 24.
[2] J. Fleig, K.D. Kreuer, J. Maier, Handbook of Advanced Ceramics, vol. 2, Elsevier, Singapore, 2003. p. 59.
[3] J. Fleig, Annu. Rev. Mater. Res. 33 (2003) 361.
[4] J. Fleig, F.S. Baumann, V. Brichzin, H.R. Kim, J. Jamnik, G. Cristiani, H.U. Habermeier, J. Maier, Fuel Cells 6 (2006) 284.
[5] R.A. Evarestov, E.A. Kotomin, Y.A. Mastrikov, D. Gryaznov, E. Heifets, J. Maier, Phys. Rev. B 72 (2005) 214411.
[6] G. Kresse, J. Furthmüller, VASP the Guide, Wien, 2003.
[7] G. Henkelman, A. Arnaldsson, H. Jonsson, Comp. Mater. Sci. 36 (2006) 354.
[8] P.W. Tasker, Philos. Mag. A 39 (1979) 119.
[9] C. Noguera, Physics of Oxide Surfaces, Cambridge University Press, NY, 1996.
[10] E. Heifets, S. Piskunov, E.A. Kotomin, Y.F. Zhukovskii, D. Ellis, Phys. Rev. B 75 (2007) 115417;
E. Heifets, R.I. Eglitis, E.A. Kotomin, J. Maier, G. Borstel, Phys. Rev. B 64 (2001).
[11] Yu. A. Mastrikov, E.A. Kotomin, E. Heifets, J. Maier, Arxiv Cond. Mater. (2008), arXiv:0807.1864v1.
[12] R.A. Evarestov, E.A. Kotomin, D. Fuks, J. Felsteiner, J. Maier, Appl. Surf. Sci. 238 (2004) 457.
[13] R.A. Evarestov, E.A. Kotomin, E. Heifets, J. Maier, G. Borstel, Solid State Commun. 127 (2003) 367.
[14] E. Heifets, W.A. Goddard III, E.A. Kotomin, R.I. Eglitis, G. Borstel, Phys. Rev. B 69 (2004) 035408.

[15] E. Heifets, R.A. Evarestov, E.A. Kotomin, S. Dorfman, J. Maier, Sens. Actuators B 100 (2004) 81.
[16] E. Heifets, E.A. Kotomin, J. Maier, Surf. Sci. 462 (2000) 19.
[17] E. Heifets, J. Ho, B. Merinov, Phys. Rev. B 75 (2007) 155431.
[18] K. Reuter, M. Scheffler, Surf. Sci. 490 (2001) 20.
[19] K. Johnston, M.R. Castell, A.T. Paxton, M.W. Finnis, Phys. Rev. B 70 (2004) 085415.
[20] J. Padilla, D. Vanderbilt, Surf. Sci. 418 (1998) 64.
[21] F. Bottin, F. Finocchi, C. Noguera, Phys. Rev. B 68 (2003) 035418.
[22] J.W. Cahn, Interfacial Segregation, American Society of Metals, Metals Park, Ohio, 1977.
[23] I. Batyrev, A. Alavi, M.W. Finnis, Faraday Discuss. 114 (1999) 33.
[24] M.W. Chase, NIST–JANAF Thermochemical Tables, American Chemical Society, Washington, DC, 1998.
[25] H. Landolt, R. Börnstein, Thermodynamic Properties of Inorganic Materials, Springer, 1999–2007.
[26] D.R. Lide, CRC Handbook of Chemistry and Physics, CRC Press, Boca Raton, 1993.
[27] E.A. Kotomin, Yu.A. Mastrikov, E. Heifets, J. Maier, Phys. Chem. Chem. Phys. 10 (2008) 4644.

Please cite this article in press as: Y.A. Mastrikov et al., Surf. Sci. (2009), doi:10.1016/j.susc.2008.11.034